Mechanics of Materials 101 (2016) 102–117

Contents lists available at ScienceDirect

Mechanics of Materials

journal homepage: www.elsevier.com/locate/mechmat

Research paper

A computational insight into void-size effects on strength properties of nanoporous materials

Stella Brach[a,c], Luc Dormieux[b], Djimédo Kondo[a], Giuseppe Vairo[a,c,*]

[a] Institut Jean Le Rond d'Alembert, UMR CNRS 7190, Université Pierre et Marie Curie, 4 Place Jussieu, F75005 Paris, France
[b] Université Paris-Est, UR Navier, UMR 8205 CNRS, Ecole des Ponts ParisTech, 6–8 av. Blaise Pascal, Cité Descartes, Champs-sur-Marne, F-77455 Marne-La-Vallée, France
[c] Dipartimento di Ingegneria Civile e Ingegneria Informatica (DICII), Universitá degli Studi di Roma "Tor Vergata", Viale Politecnico 1, 00133 Rome, Italy

ARTICLE INFO

Article history:
Received 8 April 2016
Revised 8 July 2016
Available online 20 July 2016

Keywords:
Nanoporous materials
Strength properties
Void-size effects
Lode angle influence

ABSTRACT

In this paper, strength properties of nanoporous materials are addressed aiming to establish novel insights into the influence of void-size effects. To this end, a virtual spherically-nanovoided sample of an aluminium single crystal is investigated by adopting a Molecular-Dynamics computational approach. Elasto-plastic mechanical response, under triaxial strain-based conditions and including axisymmetric and shear states, are numerically experienced, identifying the corresponding limit stresses. Computed strength measures are used to furnish estimates of strength domains, described in terms of meridian and deviatoric profiles. The influence of void-size effects on the computed strength properties is clearly quantified for different porosity levels, numerical results confirming a strengthening of the sample when the void radius reduces. Moreover, it is shown that the occurrence and the amount of void-size effects are strongly dependent on the Lode angle, resulting in a shape transition of both meridian and deviatoric strength profiles when the void radius is varied. Finally, present results suggest porosity-dependent threshold values for the void radius above which void-size effects tend to disappear. With respect to the actual state-of-the-art, useful benchmarks for assessing the effectiveness of available theoretical models are provided, resulting in a novel incremental contribution towards the definition of advanced modelling strategies for describing strength properties of nanoporous materials.

1. Introduction

In the last decades, since the development of novel and challenging nano-technologies, nanostructured materials have yielded a growing research interest, involving experimental tests, theoretical formulations and numerical models (Arico et al., 2005; Lu et al., 2004; Jenkins, 2010). An important class of nanostructured materials consists in nanoporous media, characterized by very fascinating properties or combination of properties in terms of mechanical, chemical and electromagnetic features. In particular, due to the presence of nanoscale cavities, these materials exhibit a high capability to interact, absorb and cooperate with atoms, ions and molecules. Moreover, they are characterised by reduced mass density, high surface-to-volume ratio, good levels of both stiffness and strength, and they generally exhibit a ductile behaviour. Accordingly, nanoporous materials open towards groundbreaking functional applications in several technical fields, including civil and environmental engineering, geophysics, petroleum industry, biomechanics, chemistry. For instance, they are used to conceive multifunctional devices for aerospace/automotive applications, energy storage, ion-exchange, molecular biosensing and bioseparation, drug delivery, catalysis, filtration, sensoring (Jenkins, 2010).

From a mechanical point of view, one of the most fundamental aspect consists in identifying and describing the constitutive response and the strength properties of these materials, as dependent on the size of voids (which is in the order of some nanometres), as well as on their shape and arrangement (Dormieux and Kondo, 2010; 2013; Huang et al., 2005; Li and Huang, 2005; Monchiet et al., 2008; Monchiet and Kondo, 2013). As regards void-size effects, well-established experiments (usually based on nano-indentation tests) have shown that a reduction in the length-scale of nanovoids induces an improvement of the material strength (Biener et al., 2005; 2006; Hakamada and Mabuchi, 2007). Such an effect cannot be theoretically described by classical approaches for porous materials (e.g., Gurson, 1977; Ponte Castaneda, 1991),

* Corresponding author. Fax: +390672597042.
E-mail addresses: brach@ing.uniroma2.it (S. Brach), dormieux@lmsgc.enpc.fr (L. Dormieux), djimedo.kondo@upmc.fr (D. Kondo), vairo@ing.uniroma2.it (G. Vairo).

http://dx.doi.org/10.1016/j.mechmat.2016.07.012
0167-6636/

that are generally conceived to predict porosity effects only, and thereby resulting in void-size-independent strength criteria.

The influence of void size on the mechanical behaviour of nanoporous materials are related to the presence, at the cavity boundaries, of self-equilibrated surface stresses (Needs et al., 1991). These latter can be modelled via interface laws (Gurtin and Murdoch, 1975) and they reveal fundamental in describing the mechanical response of nanoscale structures (Amelang and Kochmann, 2015) and nano-structured materials (e.g., Duan et al., 2005b,a), as well as for modelling strength properties of nanoporous media (e.g., Dormieux and Kondo, 2010; 2013; Goudarzi et al., 2010; Monchiet and Kondo, 2013; Moshtaghin et al., 2012). As an example, by applying a limit-analysis approach on a hollow spherical domain, Dormieux and Kondo (2010) extended the well-known strength criterion proposed by Gurson (1977) for ductile porous media to the case of nanoporous materials, aiming to predict void-size effects. The void-size-dependent strength criterion by Dormieux and Kondo (2010), as well as the porous model by Gologanu et al. (1993; 1994), have been successively extended by Monchiet and Kondo (2013) to the case of nanoscale spheroidal cavities, thereby incorporating both void-shape and void-size effects. Other analytical formulations have been proposed by Dormieux and Kondo (2013), Goudarzi et al. (2010), Zhang and Wang (2007) and Zhang et al. (2010), by combining non-linear homogenization techniques and variational arguments, and resulting in a generalization of the Ponte–Castaneda's strength criterion (Ponte Castaneda, 1991) to nanoporous materials.

It is worth observing that available strength models for nanoporous materials are based on a number of a priori assumptions. In fact, they generally include a very simple limit behaviour of the bulk matrix, as well as a simplified representation of the physics underlying nanoscale effects (usually faced by introducing fictitious plastic interfaces). Nevertheless, available experimental results are not sufficient to support these assumptions, so that current theoretical models can be neither properly validated nor suitably calibrated. As a matter of fact, apart from some qualitative indications of the void-size influence on the material strength level, no further information can be deduced from the experimental literature either on the three-dimensional material strength domain or on the influence of the void size as a function of the loading state. In this context, numerical methods may be considered as an effective alternative to provide comparative benchmarks, allowing also to successfully control a number of possible coupled effects, and thereby resulting in useful indications towards advanced modelling strategies.

Computational methods usually employed for modelling macro- and/or micro-mechanical response are not able to automatically provide helpful insights on nanoscale effects, since they do not include a satisfactory description of the material structure at that length-scale. On the contrary, and as confirmed by recent investigations (e.g., Bringa et al., 2010; Borg et al., 2008; Mi et al., 2011; Tang et al., 2010; Traiviratana et al., 2008; Zhao et al., 2009), numerical methods based on Molecular Dynamics (MD) approaches allow to describe the material arrangement at the atomistic level, and thereby they can be considered as promising tools for investigating the elasto-plastic behaviour of nanoporous materials.

As a matter of fact, available studies based on MD approaches mainly address the identification and the characterization of atomistic mechanisms underlying failure processes related to void growth and coalescence (e.g., Farrissey et al., 2000; Lubarda et al., 2004; Lubarda, 2011; Marian et al., 2004; 2005; Pogorelko and Mayer, 2016; Ruestes et al., 2013; Tang et al., 2010; Traiviratana et al., 2008). On the other hand and at the best of the authors' knowledge, very few attempts have been provided in order to employ these numerical strategies to furnish indications towards the definition of engineering strength measures for nanoporous materials. For instance, an attempt to put in relationship strength properties at the macroscale with MD-based evidence has been provided by Mi et al. (2011) and Traiviratana et al. (2008), referring to the void-size-independent Gurson model. Nevertheless, current MD studies are generally limited to the analysis of particular admissible stress states only, computed under uniaxial (Farrissey et al., 2000; Tang et al., 2010), volumetric or shear conditions (Marian et al., 2004; 2005), and therefore defining only few discrete points on the a-priori unknown material strength surface, without considering more complete multiaxial scenarios. In fact, a comprehensive three-dimensional characterization of material strength properties requires a proper investigation of failure mechanisms under multiaxial loading conditions. Furthermore, no numerical evidence has been yet provided concerning the influence of void size on material strength domains. Accordingly, with respect to the previously-discussed state-of-the-art, a parametric multiaxial loading strategy is expected to pave the way for a number of original contributions, such as: (i) complete identification of failure surfaces and of the influence of stress invariants on material strength properties; (ii) analysis of void-size effects on strength domains; (iii) assessment of novel and effective comparative benchmarks for validating and calibrating available theoretical formulations, as well as for drawing advanced modelling strategies.

It must be pointed out that porous and nanoporous materials may be generally characterised by irregular patterns and randomly-distributed voids. Nevertheless, as it is customary in classical elasto-plastic theoretical approaches for micro/nano-structured materials, simple geometrical descriptions are often considered. This is the case of single-voided domains and of hollow sphere models (Gurson, 1977), widely adopted in porous metal plasticity and limit analysis approaches (Dormieux and Kondo, 2010; Monchiet and Kondo, 2013; Tvergaard and Needleman, 1984). Corresponding results are strictly valid for the particular, but realistic, considered microstructure (in the case of hollow sphere models, the microstructure is the so-called Hashin Composite Sphere Assemblage, (Hashin, 1962; Leblond et al., 1994; Michel and Suquet, 1992)), but they generally furnish also helpful indications on statistically-equivalent arrangements. In this framework, domains embedding a single spherical nanovoid have been adopted in many recent MD-based computational studies (e.g. Farrissey et al., 2000; Marian et al., 2004; 2005; Traiviratana et al., 2008), addressing plastic mechanisms in nanoporous materials.

In this paper, strength properties of an aluminium single crystal containing a spherical nanovoid are addressed via a Molecular Dynamics approach. A parametric analysis with respect to the void radius and for different porosity levels is carried out, by considering different strain paths (shear, triaxial expansion and triaxial compression) and a wide range of triaxiality scenarios (from pure deviatoric conditions to pure hydrostatic ones). The computational model is defined in Section 2, drawing also basic elements of the adopted numerical procedure. With the aim to present simulation results in the framework of a customary notation in plasticity, and by referring to average stress and strain measures, the Haigh–Westergaard (HW) coordinates are introduced. Section 3 is devoted to analyse some preliminary results, in terms of both stress-strain relationships and dominant atomistic mechanisms, in order to identify suitable strength measures for estimating limit stress conditions for the in-silico samples. Analyses of numerically-experienced strength properties are provided in Section 4, wherein meridian and deviatoric representations of computed strength domains are proposed, highlighting and discussing the influence of void-size effects. Finally, main concluding remarks are traced in Section 5.

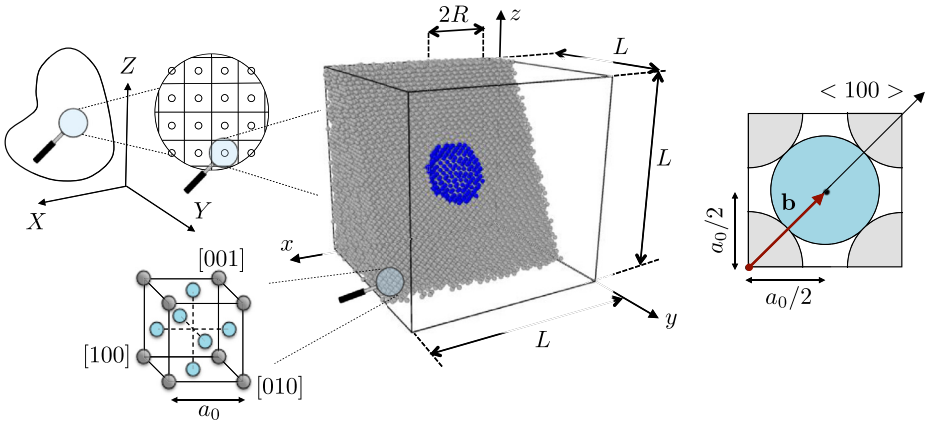

Fig. 1. Computational model herein adopted for describing an aluminium nanovoided single crystal. Notation.

2. Problem statement and computational methods

Let a material neighbourhood of a nanoporous medium be considered (Fig. 1), characterized by a periodic nanostructure along the global Cartesian directions *X, Y* and *Z*, and whose representative cell consists in a nano-single crystal embedding a single spherical void. In the following, reference is made to a single crystal of aluminium, whose ideal crystallographic arrangement is based on a face-centred cubic lattice (FCC). Let the local Cartesian frame (*x, y, z*) be introduced, with axes parallel to the global ones and with $\{\mathbf{e}_x, \mathbf{e}_y, \mathbf{e}_z\}$ the corresponding orthonormal basis. Moreover, referring to the Miller's notation (Hull and Bacon, 2001), let the orientation of FCC lattices be assumed such that crystallographic directions [100], [010] and [001] line up with axes *x, y* and *z*, respectively.

A numerical approach based on a MD strategy and implemented in LAMMPS (Large-scale Atomic/Molecular Massively Parallel Simulator) (Plimpton, 1995) is adopted, by considering a cubic simulation box (Fig. 1) undergoing periodic boundary conditions. The simulation domain is defined by: the edge length L; a centred spherical void of radius R; the atomic arrangement $\mathcal{C}^0$, resulting from the bulk FCC-based cubic box by suppressing all atoms belonging to the centred spherical region. Different values of the box length L are herein considered, such that:

$$\frac{L}{B} = 10\big(1+n\big) \tag{1}$$

n being an integer number ranging from 1 to 10, $B = a_0/2$ being the length-scale of the Burgers vector $\mathbf{b} = B\langle 110\rangle$ associated to perfect dislocations along slip directions of type $\langle 110\rangle$, and a_0 being the lattice constant (equal to 4.04 Å for aluminium at room temperature (Mishin et al., 1999)). Accordingly, for a fixed material porosity p, defined as $p = 4\pi R^3/3L^3$, varying the box length L corresponds to proportionally vary the void radius R. For instance, referring to the case $p = 1\%$, R varies from 0.541 nm to 2.977 nm when L/B varies from 20 ($n = 1$) to 110 ($n = 10$). It is worth observing that, since the cut-off distance r_c for the aluminium is equal to 0.628 nm (Mishin et al., 1999), assumption in Eq. (1) allows to satisfy the minimum image convention (Allen and Tildesley, 1991), resulting in the consistency requirement $L > 2r_c$ for any $n \geq 1$.

Vector velocities $\mathbf{v}_i$ $(i = 1 \ldots N)$ of the N atoms in $\mathcal{C}^0$ are initialized as non-physical random vectors. In order to obtain a physically-consistent simulation domain at the temperature $T^* = 300$ K and with zero pressure at the domain boundaries, a preliminary equilibration step is performed by simulating 30 picoseconds via a Nose–Hoover time-integration scheme (e.g., Plimpton, 1995). As a result, the statistically-equilibrated configuration $\mathcal{C}^*$ is obtained, consisting in a cubic simulation domain with the edge length equal to L^*. For the sake of compactness, values of L^* obtained from this preliminary equilibration step are omitted, consisting however in percentage differences with respect to L always less then 0.3%.

Afterwards, considering $\mathcal{C}^*$ as the reference configuration at the time $t = 0$, an incremental strain-driven deformation process is simulated, considering a fixed time-step Δt. Denoting with $\bar{t}$ the actual value of the time variable, a measure of the actual strain tensor for the overall simulation domain is assumed to be expressed by:

$$\mathbf{D}\big(\bar{t}\big) = \chi\bar{t}\big(D_x\mathbf{e}_x\otimes\mathbf{e}_x + D_y\mathbf{e}_y\otimes\mathbf{e}_y + D_z\mathbf{e}_z\otimes\mathbf{e}_z\big) \tag{2}$$

where χ is a positive strain-rate constant parameter, and D_x, D_y and D_z are assigned dimensionless quantities. Accordingly, the prescribed increments of the box lengths at each time-step result in $\Delta L_q = L^* D_q\,\chi\,\Delta t$, with $q = x, y, z$.

As a notation rule, the following three strain invariants are introduced: $I_1^D = \mathrm{tr}\,\mathbf{D}$, $J_2^D = \mathbf{D}_d : \mathbf{D}_d/2$ and $J_3^D = \det\mathbf{D}_d$, where $\mathbf{D}_d = \mathbf{D} - (I_1^D/3)\mathbf{1}$ is the deviatoric strain tensor and $\mathbf{1}$ is the second-order unit tensor ($1_{ij} = \delta_{ij}$, with δ_{ij} the Kronecker symbol). Moreover, referring to a strain-based Haigh-Westergaard notation (see for instance Menetrey and Willam, 1995), the strain Lode angle $\theta_D \in [0, \pi/3]$ is defined such that: $\cos 3\theta_D = 3\sqrt{3}J_3^D/[2(J_2^D)^{3/2}]$. When necessary, reference is also made to the following invariant strain measures: $D_m = I_1^D/3$ and $D_{eq} = \sqrt{J_2^D}$.

In order to analyse the sample response under a broad range of triaxial strain-based conditions, three deformation paths are simulated, corresponding to $\theta_D = 0$ (triaxial strain expansion, denoted as $\mathrm{TXE_D}$), $\theta_D = \pi/3$ (triaxial strain compression, denoted as $\mathrm{TXC_D}$), and $\theta_D = \pi/6$ (shear strain conditions, denoted as $\mathrm{SHR_D}$). Furthermore, the following choices of the dimensionless quantities D_x, D_y and D_z are considered:

$$\begin{aligned}
&\mathrm{TXE_D} \quad : \quad D_x = D_y = \lambda, \quad D_z = 1\\
&\mathrm{TXC_D} \quad : \quad D_y = D_z = 1, \quad D_x = \eta\\
&\mathrm{SHR_D} \quad : \quad D_x = 1, \quad D_y = (1+\mu)/2, \quad D_z = \mu
\end{aligned} \tag{3}$$

For any choice in Eq. (3), and referring to the case of a non-negative first invariant I_1^D, different scenarios are simulated. In detail, several strain-based triaxiality levels, ranging from a pure deviatoric condition ($D_m = 0$) to a pure hydrostatic one ($D_{eq} = 0$), are accounted for by varying the dimensionless coefficients λ, η and μ, as summarised in Table 1.

In order to achieve effective results with a reasonable computational time, numerical simulations are performed by considering $\chi = 5 \cdot 10^9$ s^{-1}. Such a strain-rate value is consistent with those usually adopted in the recent MD-based literature, ranging

Table 1
Values adopted for parameters λ, η and μ introduced in Eq. (3) to describe different triaxiality levels, ranging from a pure deviatoric condition ($D_m = 0$) to a pure hydrostatic one ($D_{eq} = 0$).

	$D_m = 0$								$D_{eq} = 0$
λ (TXE_D)	−0.5	−0.4	−0.3	−0.2	−0.1	0	0.25	0.5	1
η (TXC_D)	−2	−1.8	−1.6	−1.4	−1.2	−1	−0.5	0	1
μ (SHR_D)	−1	$-0.8\overline{6}$	$-0.7\overline{3}$	−0.6	$-0.4\overline{6}$	$-0.\overline{3}$	0	$0.\overline{3}$	1

from 10^7 to 10^{12} s^{-1} (Bringa et al., 2010; Horstemeyer et al., 2001; Mi et al., 2011; Pogorelko and Mayer, 2016; Ruestes et al., 2013; Seppala et al., 2004; Shabib and Miller, 2009; Tang et al., 2010; Traiviratana et al., 2008; Zhao et al., 2009), and it can be experimentally obtained via laser-shock techniques (Lubarda et al., 2004). As a further consistency indication for such a choice, Horstemeyer et al. (2001) numerically proved that the yield strength for FCC metals becomes practically insensitive to the strain rate for values lower than 10^{10} s^{-1}.

Adopting a time-step equal to $\Delta t = 1$ femtosecond, trajectories of atoms are determined by integrating the Newton's second law via the Verlet algorithm (Verlet, 1967). As a result, the actual average stress tensor is computed as the superposition of atomistic kinetic contributions and pairwise interactions, and it is described via the following virial formula (e.g., Subramaniyan and Sun, 2008):

$$\boldsymbol{\Sigma}(\bar{t}) = -\frac{1}{V_{at}}\sum_{i=1}^{N}\left(m_i\mathbf{v}_i\otimes\mathbf{v}_i + \sum_{j\neq i,\, j=1}^{N} f_{ij}\frac{\mathbf{r}_{ij}\otimes\mathbf{r}_{ij}}{r_{ij}}\right) \tag{4}$$

where V_{at} is the total atomic volume, m_i is the mass of the atom i, and $f_{ij} = \partial\mathcal{E}/\partial r_{ij}$ is the modulus of the interaction force between atoms i and j. The total energy $\mathcal{E}$ of the system is defined in agreement with the Embedded Atom Method (Daw and Baskes, 1984) as:

$$\mathcal{E} = \sum_{i=1}^{N} F_i\left(\overline{\rho}_i\right) + \frac{1}{2}\sum_{i=1}^{N}\sum_{j=1\neq i}^{N}\Phi_{ij}(r_{ij}), \quad \text{with} \quad \overline{\rho}_i = \sum_{j=1\neq i}^{N}\rho_j(r_{ij}) \tag{5}$$

where r_{ij} is the modulus of the separation vector $\mathbf{r}_{ij} = \mathbf{r}_j - \mathbf{r}_i$, with $\mathbf{r}_i$ identifying the position of the atom i. Accordingly, $\mathcal{E}$ is defined as the superposition of two terms. The first is the sum of cohesive embedding energies F_i (required to include the atom i into the electron cloud), expressed in terms of the electron-cloud density $\overline{\rho}_i$ (defined as the linear superposition of the neighbouring atomic electron densities ρ_j). The second contribution is associated to the repulsive pairwise potential function Φ_{ij} between the atom i and its neighbours j.

In this study, the Haigh–Westergaard (HW) representation is adopted for giving a three-dimensional description of the computed strength states. Accordingly, denoting with $\theta_\Sigma \in [0, \pi/3]$ the stress Lode angle, a given stress state $\boldsymbol{\Sigma}$ is uniquely determined by referring to the following stress-invariant quantities (e.g., Khan and Huang, 1995; Lubliner, 2008):

$$\zeta = \frac{I_1^\Sigma}{\sqrt{3}}, \qquad r = \sqrt{2J_2^\Sigma}, \qquad \cos 3\theta_\Sigma = \frac{3\sqrt{3}J_3^\Sigma}{2\left(J_2^\Sigma\right)^{3/2}} \tag{6}$$

where $I_1^\Sigma = \mathrm{tr}\,\boldsymbol{\Sigma}$, $J_2^\Sigma = \boldsymbol{\Sigma}_d : \boldsymbol{\Sigma}_d/2$ and $J_3^\Sigma = \det\boldsymbol{\Sigma}_d$ are the isotropic stress invariants, and where $\boldsymbol{\Sigma}_d = \boldsymbol{\Sigma} - (I_1^\Sigma/3)\mathbf{1}$ is the deviatoric part of the stress measure introduced in Eq. (4). For what follows, notation TXE_Σ, TXC_Σ and SHR_Σ is introduced to indicate triaxial stress expansion (i.e., $\theta_\Sigma = 0$), triaxial stress compression (i.e., $\theta_\Sigma = \pi/3$) and shear (i.e., $\theta_\Sigma = \pi/6$) stress states. Furthermore, when necessary, reference is made to the following invariant stress measures: $\Sigma_m = I_1^\Sigma/3$ and $\Sigma_{eq} = \sqrt{J_2^\Sigma}$.

The HW representation defines a cylindrical coordinate system $(\zeta, r, \theta_\Sigma)$ within the space of the principal stresses $(\Sigma_1, \Sigma_2, \Sigma_3)$, with ζ and r being the magnitudes of the orthogonal projections of the stress tensor $\boldsymbol{\Sigma}$ on the hydrostatic axis (i.e., $\Sigma_1 = \Sigma_2 = \Sigma_3$, $r = 0$) and on the deviatoric plane (or π-plane, that is $\zeta = \mathrm{const}$), respectively. It is worth to remark that, for a given stress state $(\zeta, r, \theta_\Sigma)$ it is always possible to recover the corresponding stress tensor $\boldsymbol{\Sigma}$, allowing for possible alternative representations (based for instance on anisotropic stress invariants, (Hill, 1948; Monchiet et al., 2008)). Nevertheless, aiming to furnish possible indications towards the characterization of material strength properties in the framework of a continuum description, and since actual strength models for nanoporous media are generally expressed in terms of isotropic stress invariants, the HW representation is herein considered as useful for such purposes.

3. Strength measure and atomistic mechanisms

Strength properties of the herein-considered aluminium nanovoided single crystal are identified by defining, for each deformation scenario, a limit stress state. With reference to stress and strain measures previously introduced, typical stress-strain responses computed via the present approach are shown in Figs. 2 and 3. They refer to the case $p = 1\%$ and $L/B = 50$ (corresponding to $R = 1.353$ nm) and address the deformation path TXE_D. Aiming to furnish some indications on temperature effects related to elasto-plastic mechanisms, two different cases are simulated: an isothermal process (denoted as IP), and a non-isothermal one (NIP, no temperature control is used during the loading process). Stress-strain relationships presented in Fig. 2 are obtained for three different deformation scenarios ($\lambda = -0.5$, pure deviatoric condition; $\lambda = 0$, traction test corresponding to a mixed hydrostatic/deviatoric condition; $\lambda = 1$, pure hydrostatic condition). Moreover, addressing the case $\lambda = -0.5$, Fig. 3a depicts stress-strain responses computed in the IP case for different temperature values, and Fig. 3b shows the temperature evolution numerically experienced in the NIP-based simulation.

As main features of the resulting stress-strain responses, stress peaks are clearly identified, indicating a critical condition for the sample, followed by a stress-relaxation phase. Stress-strain relationships obtained by considering all the other deformation paths and different triaxiality levels (see Eq. (3) and Table 1), as well as in the case of a bulk sample (i.e., $p = 0$), exhibit the same characteristics and they are herein omitted for the sake of compactness. With reference to the IP case and mainly resulting from the temperature influence on the atomic mobility, Fig. 3a shows that when the temperature increases then the stress peak reduces, and the latter is attained at a lower strain level. Furthermore, for high strains, material response is proven to become smoother as temperature is higher, sequences of rises and falls tending to disappear. On the other hand, addressing the NIP deformation process, Fig. 3b reveals that the occurrence of the stress peak corresponds to a significant change in the slope of the monotonically-increasing temperature evolution. Nevertheless, as it is highlighted by comparing IP- and NIP-based results (Fig. 2), such a heating does not significantly affect either the values of the stress peaks or the

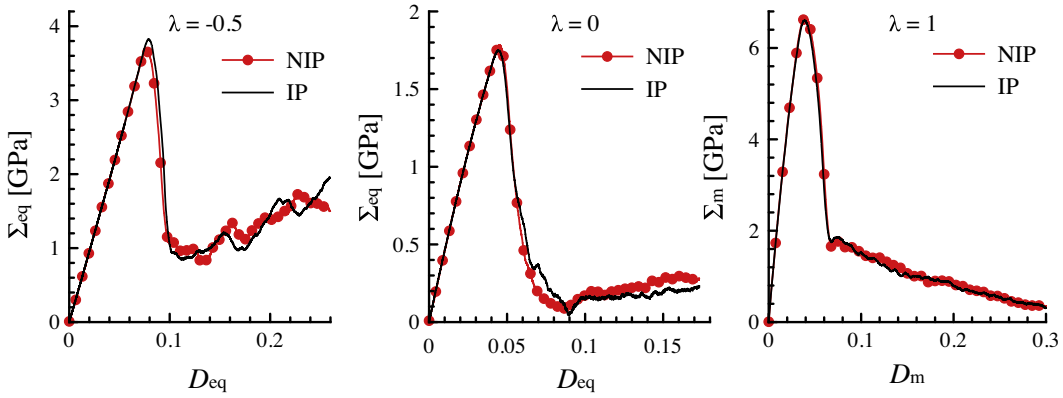

Fig. 2. Stress-strain relationships computed for the deformation path TXE_D with: $\lambda = -0.5$ (pure deviatoric state), $\lambda = 0$ (traction test) and $\lambda = 1$ (pure hydrostatic state). $L/B = 50$, $R = 1.353$ nm, $p = 1\%$. IP: isothermal process (at 300 K). NIP: non-isothermal process.

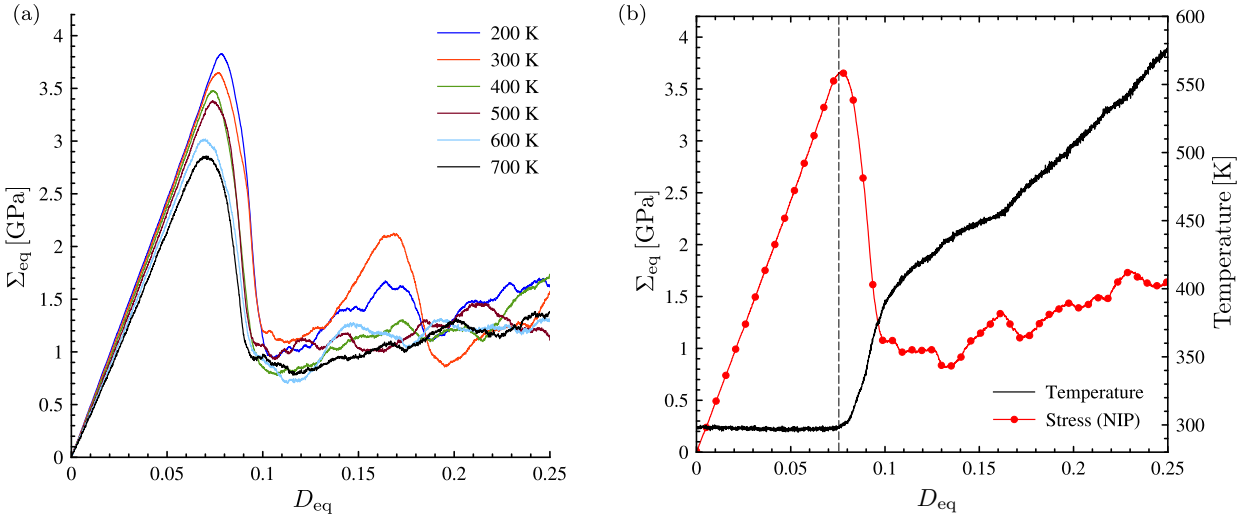

Fig. 3. Deformation path TXE_D with $\lambda = -0.5$ in the case $L/B = 50$ and for $p = 1\%$. (a) Stress-strain responses computed considering an isothermal process (IP) and for different temperature values. (b) Stress and temperature vs. strain in the case of a non-isothermal process (NIP).

strain levels at which they occur. On the contrary, some heating-induced effects appear for higher strains values.

As previously stated, very few experimental tests have been performed so far in order to characterise the mechanical response of nanoporous materials, and the corresponding evidence is thereby not sufficient to provide a proper validation benchmarking for MD-based results. Nevertheless, present numerically-experienced stress-strain features are fully in agreement with those obtained by other well-established MD studies (e.g., Mi et al., 2011; Ruestes et al., 2013; Traiviratana et al., 2008; Zhao et al., 2009).

The occurrence of the stress peak is assumed to identify the limit stress state of the sample (as also assumed, for instance, by Mi et al., 2011; Ruestes et al., 2013; Traiviratana et al., 2008; Zhao et al., 2009), and the corresponding values of stress invariants I_1^Σ, J_2^Σ and J_3^Σ allow to define a strength point $(\zeta, r, \theta_\Sigma)$ in the HW coordinate system. In the following, strength features are computed by referring to IP-based simulations.

It is worth pointing out that, when the deviatoric strain level is significant, the limit stress state of the sample is straight identified by referring to stress-strain curves expressed in terms of Σ_{eq} versus D_{eq}. On the other hand, when a pure hydrostatic deformation scenario is considered, numerical computations reveal that the stress measure Σ_{eq} is practically equal to zero, and thereby reference is made to the stress-strain response in terms of Σ_m versus D_m (Fig. 2).

Aiming to furnish indications for relating the numerically-experienced stress-strain behaviour with some basic atomistic mechanisms, MD-based results relevant to the deformation path TXE_D with $\lambda = -0.5$ (for $L/B = 50$, $p = 1\%$ and considering a NIP case) are post-processed in the OVITO environment (Stukowski, 2010), by carrying out two different analyses. The first one allows to estimate the centro-symmetry deviation parameter *CS*. This latter is defined in agreement with Kelchner et al. (1998), Stukowski (2010), and Plimpton (1995), resulting in $CS = 0$ for ideal FCC lattices (i.e., neglecting any disturbance effects induced by thermal fluctuations, (Stukowski, 2012)) and $CS > 0$ when defects, crystallographic disorder, or different lattice structures appear. The second atomistic investigation is based on the Common Neighbour Analysis (CNA) (Honeycutt and Andemen, 1987) that allows to detect the lattice nature of each atom, distinguishing among face-centered cubic (FCC), hexagonal close-packed (HCP), body-centered cubic (BCC) lattices, icosahedral (ICO) and cubic diamond (DIA) arrangements, or other assemblies with an unknown coordination structure (thereby exhibiting an amorphous nature, and denoted as "Others").

As shown in Fig. 4, due to the void presence and as a result of the preliminary equilibration step, the *CS* instantaneous measure in the reference configuration $\mathcal{C}^*$ is significantly different from 0 at the void surface, and it is characterised by values ranging from 0 to 5 elsewhere (due to thermal fluctuations).

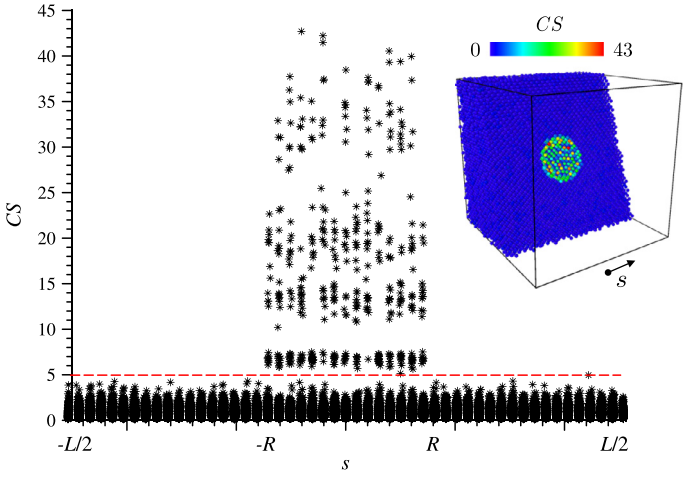

Fig. 4. Centro-symmetry distribution (*CS*), represented as one-data point per atom, relevant to the reference configuration C^*. $L/B = 50$, $R = 1.353$ nm, $p = 1\%$.

At each simulation step, the CNA post-processing phase is performed in order to investigate the evolution of the atomistic arrangement induced by the simulated deformation path, possibly associated to plastic mechanisms. Nevertheless, aiming to focus on dominant atomistic processes, the centro-symmetry parameter *CS* is used to filter regions where atomic patterns significantly differ from the FCC lattices. In detail, in agreement with previous observations, CNA post-processing is applied to atoms characterised by $CS > 5$.

The atomistic-based results obtained from the post-processing phase and depicted in the bottom part of Fig. 5, highlight that a number of dislocation mechanisms, theoretically expected for FCC-based nanovoided single crystals (as briefly summarised in Appendix A), are properly caught by the proposed simulations in the case of a pure deviatoric deformation scenario. Observed evidence is in agreement with other well-established numerical studies (e.g., Bringa et al., 2010; Marian et al., 2004; 2005; Tang et al., 2010; Traiviratana et al., 2008; Zhao et al., 2009). For instance, Marian and co-workers have obtained similar results studying the void growth of an aluminium nanovoided specimen, in terms of both volume expansion (Marian et al., 2004) and applied shear angle (Marian et al., 2005). Moreover, the herein observed dislocation nucleation and propagation mechanisms are comparable with results proposed by Traiviratana et al. (2008) and relevant to the case of an uniaxial expansion of monocrystalline and bicrystalline copper.

As a matter of fact, the analysis of Fig. 5 reveals that for small values of the equivalent strain measure D_{eq}, the sample is almost totally composed by FCC lattices and the temperature is practically constant, resulting in the elastic behaviour observed in the zone z1. At the end of this phase, for greater values of D_{eq}, proposed results show that Shockley partial dislocations are nucleated, leading to the occurrence of HCP atoms (see Appendix A). Correspondingly, a plastic regime is activated (zone z2) and the temperature slope significantly changes, in agreement with (Ruestes et al., 2013). Once nucleated at the end of the zone z1, leading Shockley partials glide away from the surface of the void until they intersect along a crystallographic direction belonging to ⟨110⟩ (see Fig. 5a), resulting in a Lomer–Cottrell dislocation. The latter is sessile and it acts as a barrier with respect to trailing partials (the so-called Lomer–Cottrell lock (Hull and Bacon, 2001)). Contemporaneously, secondary slipping systems are activated in other regions of the void surface. At the end of the zone z2 a stress peak is observed when the sessile arrangement breaks up (Fig. 5e), realising potential hotbeds for further dislocations slipping (Fig. 5f) and leading to complex dislocations interactions. In the zone z3, the stress-strain relationship experiences a relaxation phase, characterized by a steep dropping off of the stress, followed by further rises and falls associated to the formation, interaction and subsequent unlocking of other sessile assemblies, out of the current concern. Correspondingly, a significant irreversible heating appears, as both experimental (e.g., Rittel et al., 2006) and computational (e.g., Higginbotham et al., 2011) evidence widely confirms.

It is worth pointing out that plastic deformation can be accompanied at the nanoscale by a number of other complex atomistic interacting processes, related to void growth and collapse mechanisms, dislocations emission, and shear loops (Bringa et al., 2010; Marian et al., 2004; 2005; Traiviratana et al., 2008). Nevertheless, aiming to support the choice of a suitable strength measure via a basic description of atomistic mechanisms only, the detailed analysis of such phenomena does not fall in the purposes of the present study.

4. Strength analyses

Strength points computed in agreement with considerations traced in Section 3 are used to furnish meridian (i.e., in the plane (ζ, r), with $\theta_\Sigma = \text{const}$) and deviatoric (i.e., in the plane (r, θ_Σ), with $\zeta = \text{const}$) representations of the strength domain. To this aim, a non-linear least-squares fitting based on the algorithm proposed by Levenberg (1944) and Marquardt (1963) is employed.

With reference to the simulation cell introduced in Fig. 1, the presence of the nanovoid is expected to induce a perturbation on the mechanical behaviour with respect to the bulk sample (namely, corresponding to $p = 0$). Accordingly, as an useful comparative benchmark, strength properties of the in-silico bulk specimen are preliminarily investigated. Furthermore, the influence of the nanovoid on both strength-domain shape and strength values is analysed, highlighting and discussing void-size effects, when different porosity levels are accounted for.

4.1. Bulk sample

Stress-strain curves obtained in the case of a bulk domain and for different values of the simulation box length L/B are depicted in Fig. 6, addressing the deformation path TXE_D and different triaxiality levels.

As a matter of fact, the long-range nature of dislocation fields results in the interaction of dislocations through the cell boundaries, leading to possibly non-negligible periodic image effects. These latter are expected to be more significant when the box length is small. Such an occurrence is clearly highlighted by results proposed in Fig. 6, where significant differences in the material mechanical response occur within the full plastic regime (namely, in the zone z3 introduced in Fig. 5). In detail, and as a result of periodic image effects, small values of L/B induce marked sequences of rises and falls, characterised by average stress levels which are higher than those obtained for large L/B. Nevertheless, periodic image effects are proven to negligibly affect the adopted strength measure, irrespective of the considered triaxiality levels. In detail, Fig. 7a confirms that in the case TXE_D, computed strength states are almost coincident when the box length is varied, resulting in negligible discrepancies. Thereby, in the following the average results obtained for different L/B will be considered as representative of strength states for the bulk sample. Similar observations can be provided for TXC_D and SHR_D deformation paths, whose results are herein not reported for the sake of compactness.

Fig. 7b depicts strength results in the deviatoric plane (π-plane), highlighting that cross sections of the strength domain at different ζ coordinates are characterised by a triangular shape.

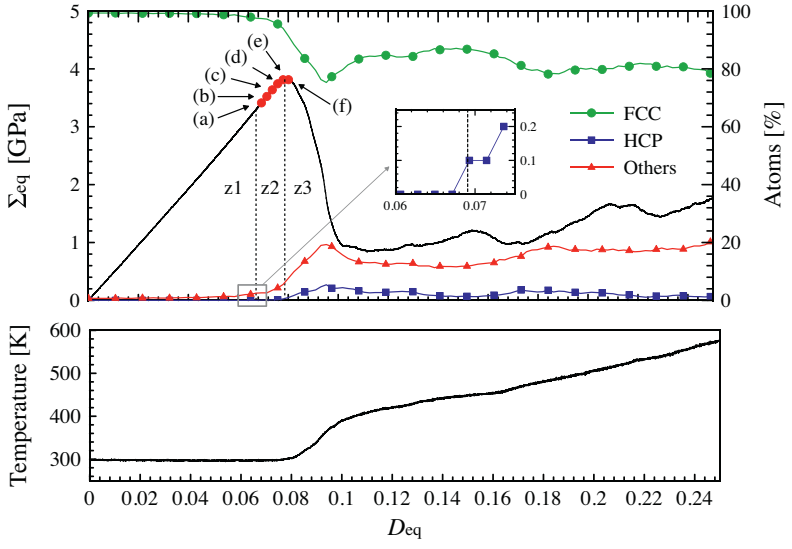

	(a)	(b)	(c)	(d)	(e)	(f)
Others	4.1 %	4.6 %	5.6 %	6.5 %	8.5 %	9.8 %
FCC	95.7 %	95.1 %	94.0 %	92.8 %	90.2 %	88.1 %
HCP	0.2 %	0.2 %	0.3 %	0.6 %	1.1 %	1.9 %
BCC	0.1 %	0.1 %	0.1 %	0.1 %	0.2 %	0.2 %

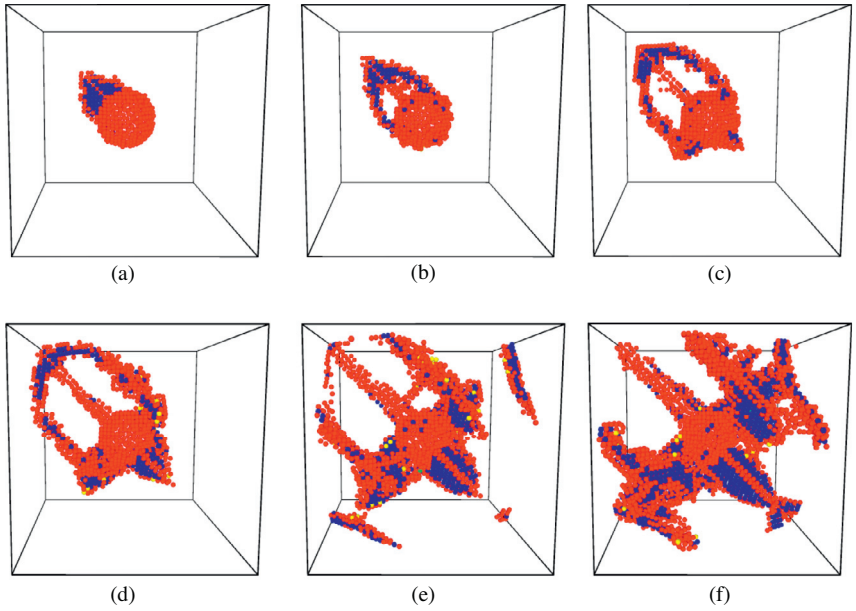

Fig. 5. (Top) Stress-strain relationship, temperature-strain relationship, and CNA results computed under a pure strain-based deviatoric condition corresponding to a non-isothermal deformation path TXE_D ($\lambda = -0.5$, $L/B = 50$, $R = 1.353$ nm, $p = 1\%$). z1: elastic zone; z2: activation of plastic mechanisms; z3: stress-relaxation zone. (Bottom) Atomic patterns and CNA results corresponding to different states within zones z2 and z3. Percentages of icosahedral (ICO) and cubic diamond (DIA) atomic arrangements are equal to zero.

Accordingly, proposed results clearly show the significant influence of all the three stress invariants I_1^Σ, J_2^Σ and J_3^Σ. Furthermore, the analysis of Fig. 7a indicates that strength states computed under pure strain-based deviatoric conditions ($\lambda = -0.5$, $\eta = -2$, $\mu = -1$, see Table 1) exhibit non-negligible hydrostatic stress components.

Table 2 summarizes computed values of the stress Lode angle θ_Σ for different deformation paths and for several values of ζ. As also shown in Fig. 7b, the axisymmetric strain conditions TXE_D ($\theta_D = 0$) and TXC_D ($\theta_D = \pi/3$) generate stress states which are in turn almost axisymmetric and characterised by $\theta_\Sigma \approx \theta_D$. Thereby, triaxial strain expansion TXE_D (respectively, compression TXC_D) practically corresponds to triaxial stress expansion TXE_Σ (respectively, compression TXC_Σ), irrespective of the value assumed for ζ. In contrast, in the case of SHR_D ($\theta_D = \pi/6$), the computed values of θ_Σ are significantly different from θ_D. As a result, SHR_D strain condition does not induce a pure shear stress state SHR_Σ (namely, corresponding to $\theta_\Sigma = \pi/6$). This occurrence has been

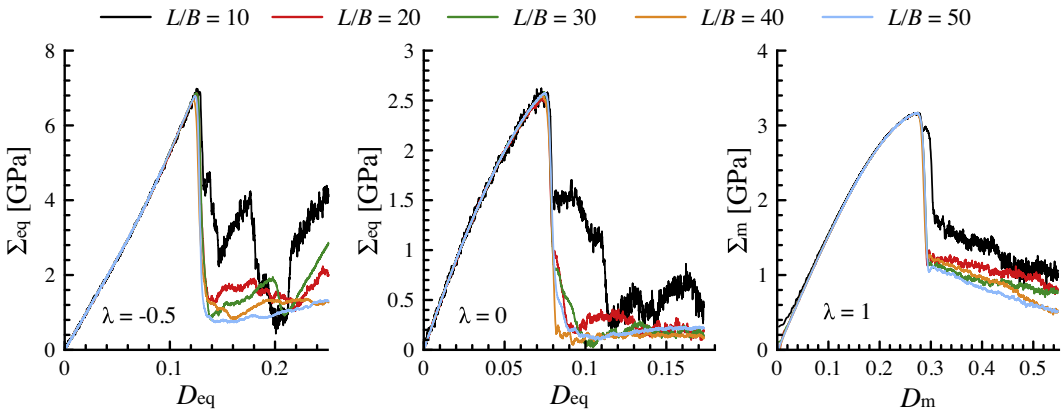

Fig. 6. Bulk sample. Influence of the simulation box length L/B on the stress-strain response for the deformation path TXE_D, for different values of λ.

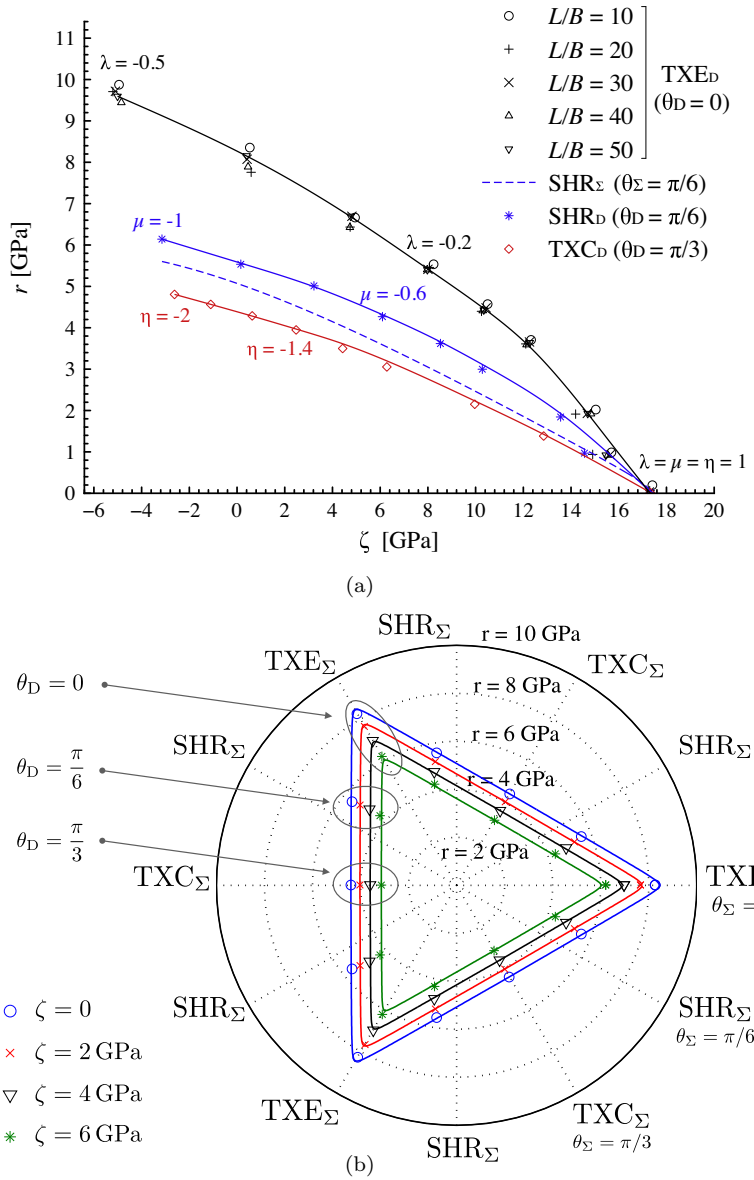

Fig. 7. Bulk sample. Strength states computed under TXE_D, TXC_D and SHR_D deformation paths. (a) Meridian strength profiles. (b) Deviatoric strength profiles. Symbols denote computed strength states, curves indicate estimated strength profiles.

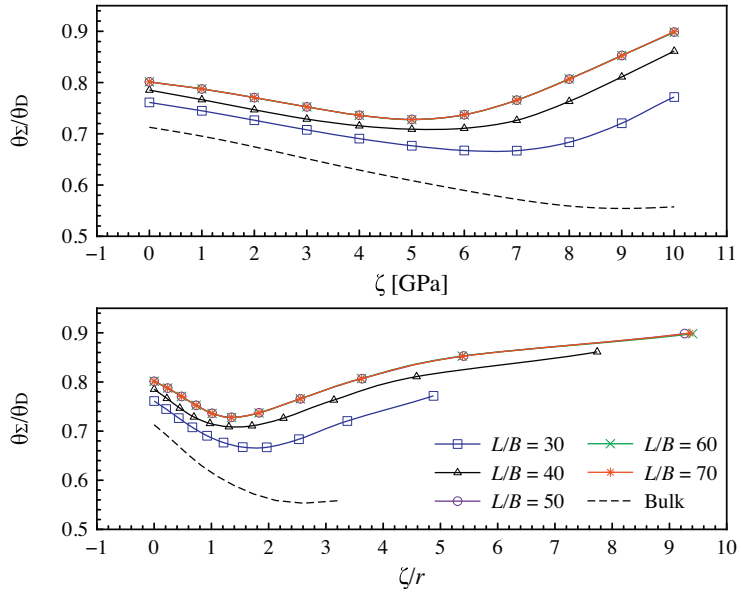

Fig. 8. Values of the stress Lode angle θ_Σ (normalised with respect to the corresponding value of θ_D) versus ζ (top) and ζ/r (bottom), computed for a nanovoided sample ($p = 1\%$) undergoing the SHR_D deformation path, and for different ratios L/B. The case of the bulk specimen is also reported.

Table 2
Bulk sample. Values of the stress Lode angle θ_Σ (normalised with respect to the corresponding values of θ_D for deformation paths SHR_D and TXC_D) for different hydrostatic stress levels.

	TXE_D	SHR_D	TXC_D
ζ [GPa]	θ_Σ [rad]	θ_Σ/θ_D	θ_Σ/θ_D
0	0.0018	0.7122	0.9969
1	0.0014	0.6961	0.9966
2	0.0012	0.6746	0.9963
3	0.0011	0.6512	0.9961
4	0.0011	0.6290	0.9961
5	0.0014	0.6087	0.9963
6	0.0019	0.5898	0.9967
7	0.0024	0.5722	0.9972
8	0.0028	0.5586	0.9979
9	0.0027	0.5531	0.9984
10	0.0025	0.5584	0.9987

also observed by Lemarchand et al. (2015), as associated to the dependency of strength properties on all the three stress invariants.

Accordingly, addressing Fig. 7a, estimated curves for strength states relevant to the TXE_D and TXC_D cases straight correspond to the intersections of the strength domain with meridian planes $\theta_\Sigma = 0$ and $\theta_\Sigma = \pi/3$, respectively. On the contrary, an estimate of the strength profile in the meridian plane $\theta_\Sigma = \pi/6$ (dashed curves) is obtained by interpolating numerical results computed by varying θ_D.

4.2. Nanovoided sample

Figures 8 to 12 summarize numerical results relevant to strength analyses on nanovoided samples, for a fixed value of porosity ($p = 1\%$) and for different values of the ratio L/B (this corresponds to proportionally vary the void radius). The case of the bulk sample is also reported for comparison, when necessary.

As in the case of the bulk sample, MD-based analyses have revealed that axisymmetric deformation paths practically result in axisymmetric stress states, leading to $\theta_\Sigma \approx \theta_D$, (see for instance Figs. 9 and 10). On the other hand, a significant discrepancy between stress- and strain-based Lode angles is observed for the deformation path SHR_D, as depending on: the Haigh–Westergaard coordinate ζ (that is, on the hydrostatic stress level), the triaxiality parameter ζ/r, and the ratio L/B (Fig. 8). Such an evidence on a nanovoided sample is in agreement with theoretical findings proposed by Lemarchand et al. (2015), obtained for a solid phase that obeys to a strength criterion depending on all the three stress invariants.

Referring to Fig. 8, two main effects can be highlighted. Firstly, the presence of a nanovoid tends to reduce the difference between θ_Σ and θ_D with respect to the bulk case, mainly for high values of hydrostatic stress and triaxiality levels. Secondly, for a fixed value of ζ, a reduction in the void size induces an increment of the discrepancy between θ_Σ and θ_D, especially for a high hydrostatic stress amount. Such an influence of the void radius tends to disappear for values of L/B greater than 50 (that is, for $R > 1.353$ nm).

As a general remark, the computed stress state does not systematically correspond to the applied strain one. Such an occurrence is also evident in meridian planes (Figs. 11 and 12), where non-negligible hydrostatic stress components can be observed when pure strain-based deviatoric conditions are considered.

The analysis of Figs. 9 to 12 suggests a clear dependence of the numerically-estimated strength properties on all the three stress invariants previously introduced. As a matter of fact, the influence on I_1^Σ and J_2^Σ can be mainly observed by referring to meridian representations in Figs. 11 and 12, as well as the dependency on J_3^Σ is highlighted by addressing the non circular profiles in π-planes of Figs. 9 and 10.

With respect to the actual state-of-the-art, this evidence confirms that a proper characterization of strength properties for nanoporous materials can be still considered as an open and challenging issue. In fact, the influence of the stress invariants is not accurately taken into account in current available theoretical models (e.g., Dormieux and Kondo, 2010; 2013; Goudarzi et al., 2010; Zhang and Wang, 2007; Zhang et al., 2010), resulting in an unsatisfactory description of the material strength domain. For instance, non-linear homogenization-based criteria by Zhang and Wang (2007) and Zhang et al. (2010) describe the meridian strength profile as elliptic, and any dependency on the

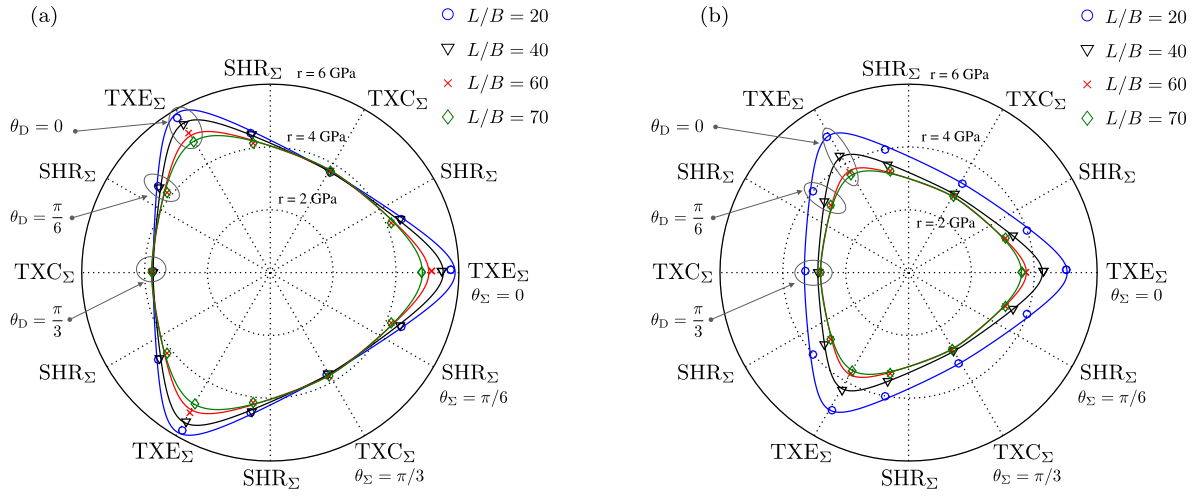

Fig. 9. Nanovoided sample ($p = 1\%$). Numerical results (symbols) and estimated strength profiles in the π-plane. (a) $\zeta = 2$ GPa. (b) $\zeta = 6$ GPa.

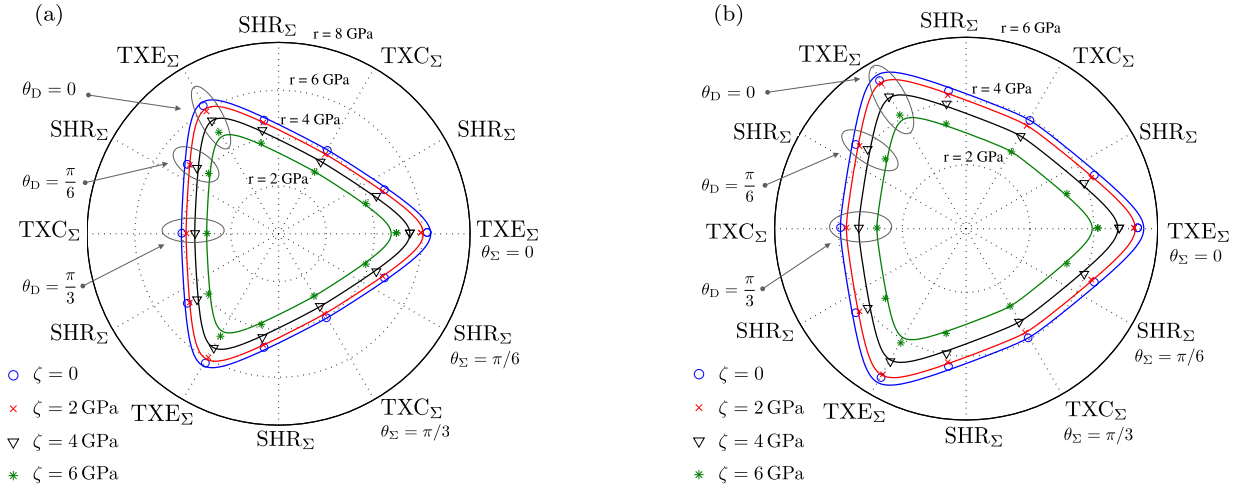

Fig. 10. Nanovoided sample ($p = 1\%$). Numerical results (symbols) and estimated deviatoric strength profiles for different hydrostatic stress levels. (a) $L/B = 30$ ($R = 0.812$ nm). (b) $L/B = 50$ ($R = 1.353$ nm).

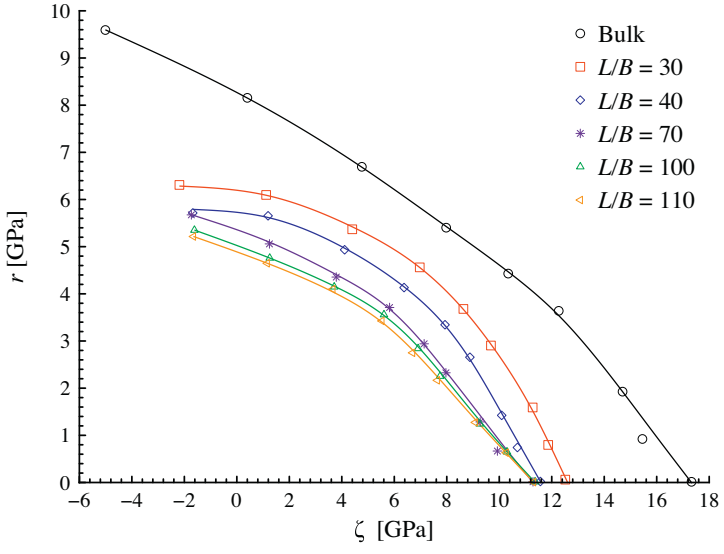

Fig. 11. Nanovoided sample ($p = 1\%$). Numerical results (symbols) and estimated meridian strength profiles for different values of L/B and for a TXE_Σ state ($\theta_\Sigma = 0$). The bulk case is also reported.

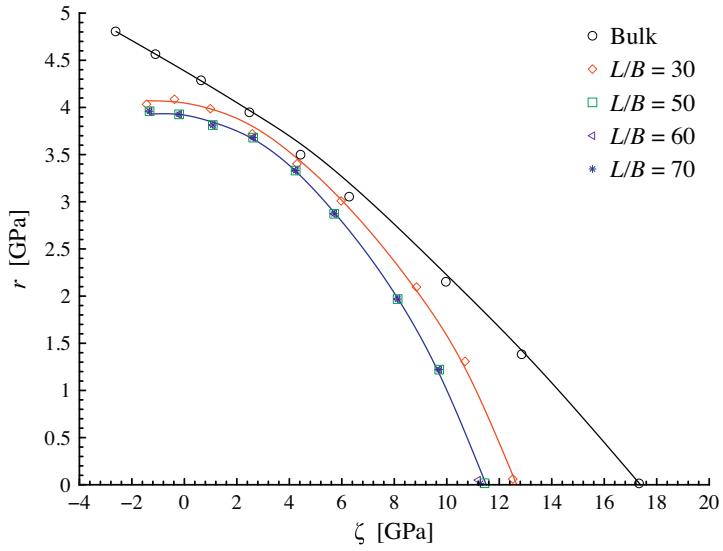

(a)

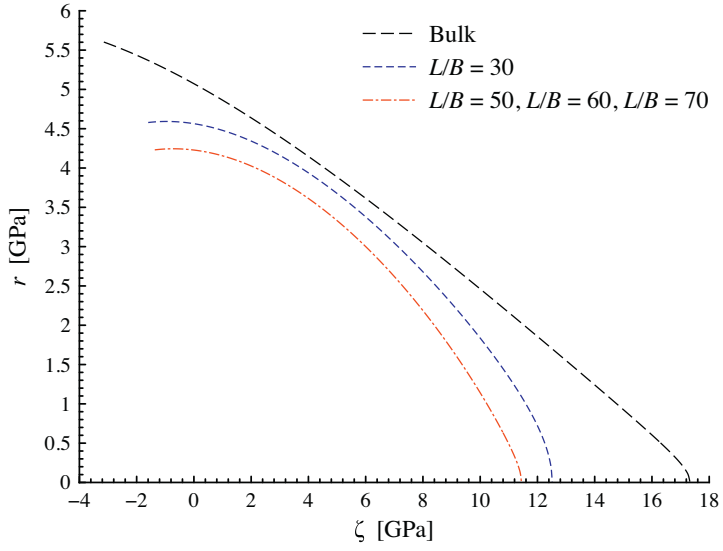

(b)

Fig. 12. Nanovoided sample ($p = 1\%$). Numerical results (symbols) and estimated meridian strength profiles for different values of L/B. (a) TXC_Σ ($\theta_\Sigma = \pi/3$). (b) SHR_Σ ($\theta_\Sigma = \pi/6$). The bulk case is also reported. As for the bulk sample, curves for SHR_Σ case are obtained by interpolating numerical results computed by varying θ_D.

third stress invariant is not accounted for (thereby resulting in a circular deviatoric strength profile). This is clearly in contrast with the obtained results, confirming that MD simulations open towards novel insights for developing and validating more effective theoretical approaches.

Proposed meridian and deviatoric strength profiles are shown to be significantly affected by void-size effects, mainly resulting in the improvement of the strength properties when the void radius reduces. Occurrence and amount of such a strengthening effect strongly depend on the value assumed by the stress Lode angle, as it clearly appears in Figs. 9, 11 and 12. In detail, referring to Fig. 9 and for a fixed hydrostatic stress level ζ, the highest influence is observed in the case of a triaxial expansion. Moreover, a shape transition is observed in the deviatoric profiles, these latter passing from a multi-sided polygonal shape to a triangular-like one when the void size reduces. Equivalently, an increase of the ratio L/B tends to mitigate the influence of the third stress invariant. This shape-transition is observed for any hydrostatic coordinate ζ, and it is associated to void-size effects only. In fact, when the void radius is fixed, the shape of π-plane strength profiles is proven to be constant with respect to ζ (Fig. 10).

Referring to meridian strength profiles depicted in Fig. 11, it is also observed that, in the TXE_Σ case, the lower the ratio L/B the higher the values of the profiles mean curvature are. Such a shape-transition effect practically does not occur in TXC_Σ and SHR_Σ meridian planes.

As a quantitative indication, when the void radius is reduced from 2.977 nm ($L/B = 110$) to 0.812 nm ($L/B = 30$), the strength measure Σ_{eq} at $\zeta = 4$ GPa (resp., $\zeta = 8$ GPa) increases of about: 40% (resp., 105%) for TXE_Σ (see Fig. 11); 5% (resp., 20%) for TXC_Σ (see Fig. 12a); 11% (resp., 18%) for SHR_Σ (see Fig. 12b). Nevertheless, computed results for $p = 1\%$ prove that strength properties

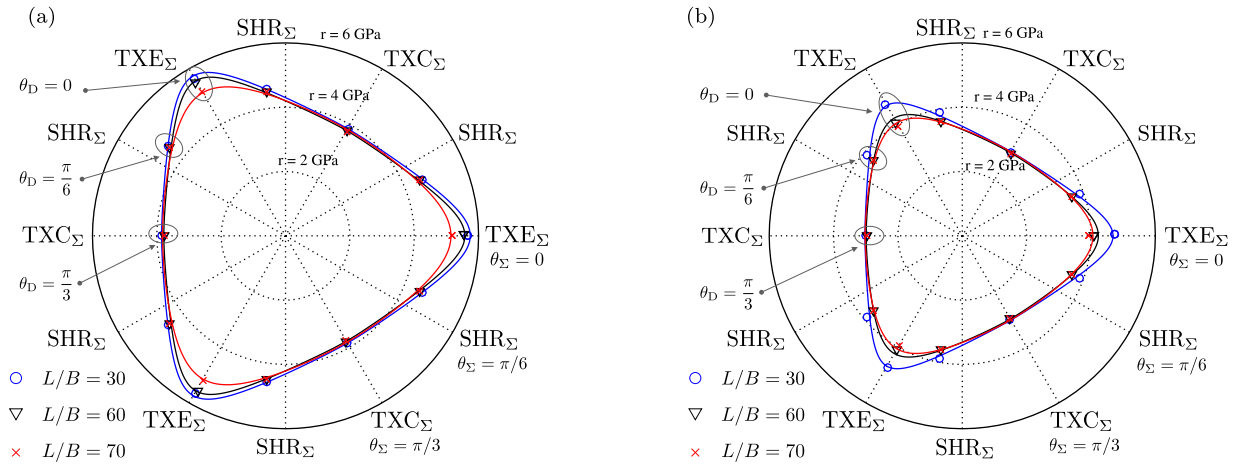

Fig. 13. Nanovoided sample ($p = 0.5\%$). Numerical results (symbols) and estimated deviatoric strength profiles in the π-planes for different values of L/B. (a) $\zeta = 2$ GPa. (b) $\zeta = 6$ GPa.

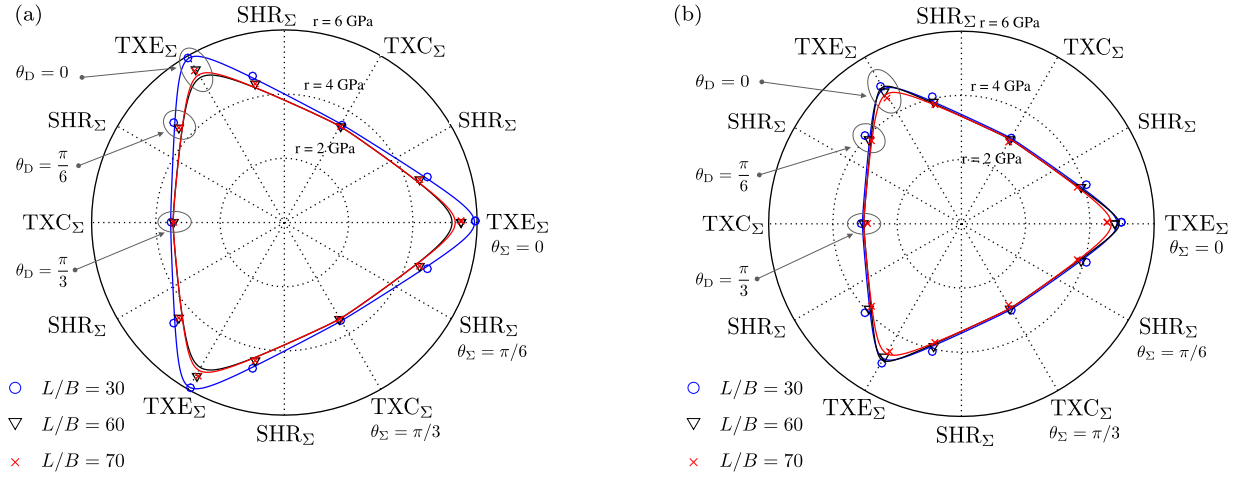

Fig. 14. Nanovoided sample ($p = 0.1\%$). Numerical results (symbols) and estimated deviatoric strength profiles in the π-planes for different values of L/B. (a) $\zeta = 2$ GPa. (b) $\zeta = 6$ GPa.

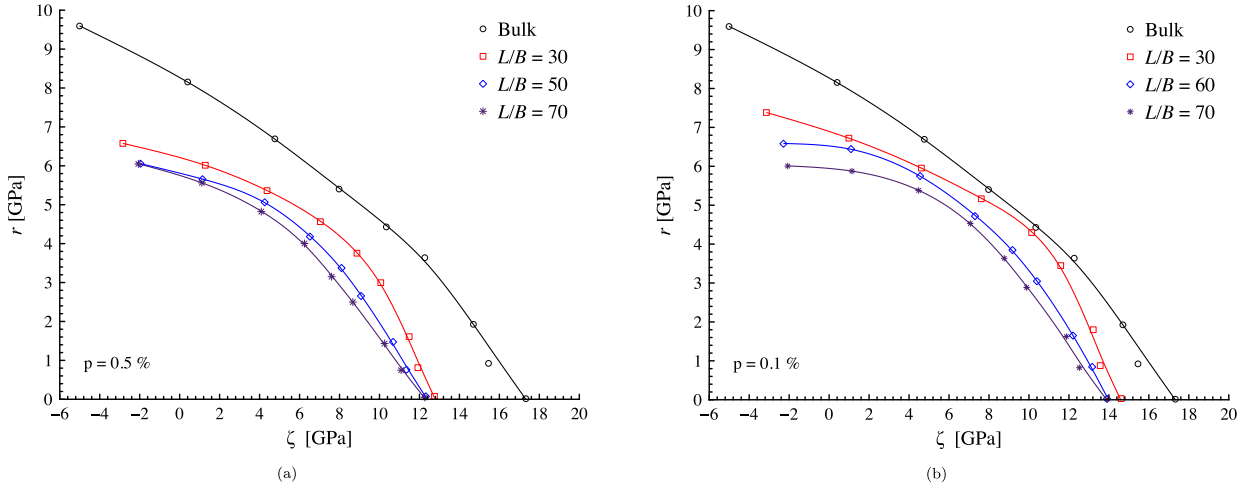

Fig. 15. Nanovoided sample. Numerical results (symbols) and estimated meridian strength profiles for different values of L/B and for a TXE$_\Sigma$ state ($\theta_\Sigma = 0$). (a) $p = 0.5\%$. (b) $p = 0.1\%$.

turn out to be almost independent from the void radius for values greater than 2.7 nm (i.e., for L/B greater than about 100) in the case TXE$_\Sigma$, and for values greater than 1.35 nm (i.e., L/B greater than about 50, Fig. 12) in the cases SHR$_\Sigma$ and TXC$_\Sigma$.

The influence of the porosity p on meridian and deviatoric strength profiles is shown in Figs. 13 to 15, relevant to porosity values $p = 0.1\%$ and $p = 0.5\%$. As expected, when p is reduced strength properties tend to increase towards the bulk ones. As in the case of $p = 1\%$, Figs. 13 and 14 reveal that axisymmetric strain-rate conditions TXE$_D$ and TXC$_D$ practically correspond to triaxial expansion and compression stress states, respectively, leading to $\theta_D \approx \theta_\Sigma$. In contrast, in the case of SHR$_D$, the computed values of

θ_Σ are significantly different from θ_D. Comparisons among results obtained for different porosity levels suggest that discrepancies between θ_Σ and θ_D tend to reduce when porosity increases. Moreover, the occurrence of a strengthening void-size effect, previously-described for $p = 1\%$, is confirmed by results in Figs. 13 ($p = 0.5\%$) and 14 ($p = 0.1\%$), where material strength properties are proven to increase when the void radius is reduced. As already observed in Figs. 9 and 10, the increase of the void radius (i.e., of L/B) leads to a shape transition of deviatoric strength profiles, almost irrespective of porosity level. Since the highest amount of the strengthening void-size effect occurs for TXE_Σ stress states, only the corresponding meridian planes are reported in Fig. 15, for the sake of compactness. As a quantitative indication and referring to the TXE_Σ case, for $p = 0.5\%$ (resp., $p = 0.1\%$) a reduction in the void radius from 1.49 nm (resp., 0.87 nm, $L/B = 70$) to 0.64 nm (resp., 0.37 nm, $L/B = 30$) induces an increase in the strength measure Σ_{eq} of about 16% (resp., 13%) for $\zeta = 4$ GPa and of about 43% (resp., 39%) for $\zeta = 8$ GPa.

5. Conclusions

In this paper the influence of void-size effects on strength properties of nanoporous materials is focused by numerically-experiencing, via a Molecular Dynamics approach, the mechanical response of a spherically-nanovoided aluminium single crystal. The case of a bulk sample (namely, with a null porosity) is preliminarily investigated aiming to furnish a comparative benchmark.

Although many MD-based analyses on nanoporous in-silico samples have been recently established, they are usually limited to the study of specific loading cases (uniaxial, volumetric or simple shear tests), mainly focusing on the identification of void-growth mechanisms and dislocation interactions, without providing an effective quantification of void-size effects. In detail, available results are sufficient neither to furnish a three-dimensional description of the corresponding strength domains (since they identify only particular stress limit conditions), nor to establish the influence of void size as depending on the loading state, thereby not allowing for a straight correlation towards the definition of engineering strength measures for nanoporous materials. Similarly, current experimental evidence, mainly related to simple testing scenarios, does not provide suitable indications on failure mechanisms under multiaxial loading conditions. Therefore, available findings can not be considered useful tools for properly assessing the effectiveness of theoretical descriptions of strength features for nanoporous materials.

With the aim to give novel contributions in this context, more complex scenarios have been herein addressed, involving triaxial strain-based expansion and compression, as well as shear strain conditions. For each case, different triaxiality levels have been considered, describing deformation paths ranging from pure deviatoric states to pure hydrostatic ones. For different porosity levels, strength properties of nanoporous samples have been investigated as a function of the void radius, in order to explore the influence of the void size.

Although available experimental data are not sufficient to provide an effective comparative benchmark, present numerical results have been proven to be fully consistent with findings obtained via other MD-based approaches (Bringa et al., 2010; Marian et al., 2004; 2005; Mi et al., 2011; Ruestes et al., 2013; Tang et al., 2010; Traiviratana et al., 2008; Zhao et al., 2009), in terms of stress-strain relationships, as well as of dominant atomistic mechanisms and irreversible heating occurring in the plastic regime.

For the cases under investigation, estimates of strength domains have been proposed. The classical Haigh-Westergaard representation, expressed by the three isotropic stress invariants, has been employed.

As main aspects, the analysis of meridian and deviatoric strength profiles computed for different porosity values has shown:

- a clear influence of all the three stress invariants;
- a complex relationship between the applied strain states and the obtained strength ones;
- significant void-size effects.

In detail, numerical results have proven that an axisymmetric stress state is obtained when axisymmetric strain conditions are applied to the sample, corresponding to practically-coinciding stress- and strain-based Lode angles. This is not the case when shear numerical tests are performed, resulting in significant differences between applied-strain and computed-stress Lode angles. Such a constitutive response at limit states is in agreement with recent theoretical findings (Lemarchand et al., 2015).

Similar effects have been also observed for the strength profiles in the meridian planes, where non-negligible hydrostatic stress components are obtained when pure deviatoric deformation paths are considered.

Furthermore, numerical results confirmed that a reduction in the void size induces an enhancement of the strength properties. This is qualitatively in agreement with available experimental (Biener et al., 2005; 2006; Hakamada and Mabuchi, 2007) and numerical (e.g., Mi et al., 2011; Traiviratana et al., 2008; Zhao et al., 2009) findings, although these latter have been obtained by considering different testing conditions, geometries and materials.

Both occurrence and amount of void-size effects have been proven as strongly dependent on the Lode angle, resulting in the highest strengthening for a triaxial expansion, and leading to a shape-transition of deviatoric strength profiles when the void radius is varied.

It is worth pointing out that, in the framework of an ideal periodic nanostructure, the single-crystal and single-voided reference domain herein adopted could be considered as not properly representative of realistic experimental samples. Nevertheless, within the limitations of the present approach, the herein-adopted computational domain enables to limit as much as possible any coupling effect (such as effects associated to: shape of voids, porosity level, polycrystalline domains), allowing to focus on dominant influence of void-size effects only.

As a matter of fact, in a number of nanoporous strength models (e.g., Dormieux and Kondo, 2010; 2013; Goudarzi et al., 2010; Monchiet and Kondo, 2012; Zhang et al., 2010), the influence of the third stress invariant is not accounted for, and solid phase is generally assumed to obey to a von Mises strength criterion (namely, independent also from the first stress invariant). Moreover, as regards the analytical description of void-size effects, it usually requires some model parameters that have to be properly calibrated and physically interpreted. In this context, proposed numerical results, both for bulk and nanoporous cases, clearly indicate a significant dependence of strength states from all the three stress invariants, suggesting the need of improving previously-cited theoretical descriptions. Furthermore, quantitative indications provided by the present approach allow to highlight some mechanical meanings of theoretical model parameters, enabling also to establish their physically-consistent ranges of variation.

Accordingly, present numerical study can be considered as an useful and novel contribution to provide comparative benchmarks for validating and calibrating available theoretical formulations, as well as for drawing novel analytical models towards a comprehensive and consistent description of nanoporous materials strength properties. As an example, in order to pave the way to more effective theoretical modelling strategies, able to reproduce available evidence, a richer description of the bulk strength behaviour with respect to the von Mises one (namely, accounting for the influence of all the stress invariants) should be addressed. In this way,

an effective description of the influence of the third stress invariant combined with void-size effects would be accounted for in the context of a general plastic behaviour.

Acknowledgments

This work was supported by Sorbonne Universités, in the framework of the PACHA program 2015 (Programme d'Accueil de Chercheurs de HAut niveau). The authors gratefully acknowledge Dr. Boris Mantisi for his technical help in Molecular Dynamics numerics.

Appendix A. Crystallographic background

Notation based on Miller indexes (Hull and Bacon, 2001) is used. As indicated by Marian et al. (2005) and Traiviratana et al. (2008), in the case of a spherical voided FCC-based sample the maximum of the resolved shear stress is reached in planes {111} embedding the void and angled by ± 45° with respect to the sample local axes. Besides, since the energy stored in a dislocation is proportional to the modulus of its Burgers vector, the glide of perfect dislocations characterized by $\mathbf{b} = B\langle 110\rangle$ is energetically disfavoured (Hull and Bacon, 2001). Referring for instance to closed packed planes (111) and (11$\bar{1}$) in Fig. A.1a, let

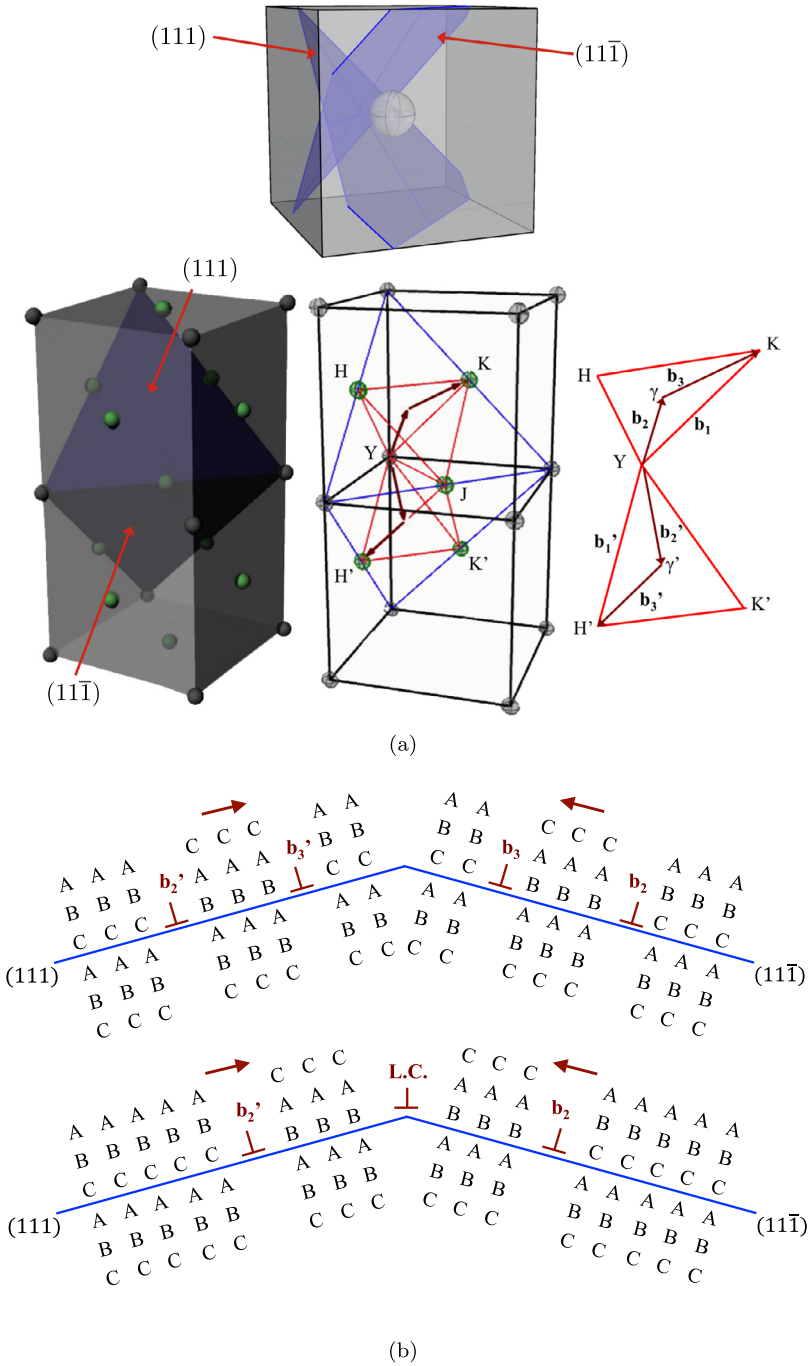

Fig. A.1. (a) An example of Shockley-partials nucleation. Perfect dislocations $\mathbf{b}_1$ and $\mathbf{b}_1'$ dissociate into partials, namely leading partials $\mathbf{b}_3$ and $\mathbf{b}_3'$, and trailing partials $\mathbf{b}_2$ and $\mathbf{b}_2'$. (b) Leading partials $\mathbf{b}_3$ and $\mathbf{b}_3'$ modify the local stacking sequence of closed packed planes {111} from FCC (sequence ABC-ABC) into HCP (sequence AB-AB). On the contrary, trailing partials $\mathbf{b}_2$ and $\mathbf{b}_2'$ remove the fault, restoring the original FCC lattice. L.C.: Lomer–Cottrell lock.

two perfect dislocations $\mathbf{b}_1 = B[101]$ and $\mathbf{b}'_1 = B[01\bar{1}]$ be considered, belonging to the Thompson tetrahedrons HKJY and H'K'JY, respectively. In agreement with energetic arguments discussed by Hull and Bacon (2001), atom in Y, instead of moving directly in K through $\mathbf{b}_1$, moves firstly in the nearby site γ (via $\mathbf{b}_2$) and next in K (via $\mathbf{b}_3$), γ being such that $\overline{Y\gamma} = \overline{\gamma K}$. As a result, the perfect dislocation $\mathbf{b}_1 = B[101]$ dissociates into two Shockley partials in the plane $(11\bar{1})$, according to the following decomposition:

$$\mathbf{b}_1 = \frac{B}{3}[112] + \frac{B}{3}[2\bar{1}1] = \mathbf{b}_2 + \mathbf{b}_3 \tag{A.1}$$

Likewise, the perfect dislocation $\mathbf{b}'_1 = B[01\bar{1}]$ dissociates into Shockley partials $\mathbf{b}'_2$ and $\mathbf{b}'_3$, both belonging to the plane (111):

$$\mathbf{b}'_1 = \frac{B}{3}[11\bar{2}] + \frac{B}{3}[\bar{1}2\bar{1}] = \mathbf{b}'_2 + \mathbf{b}'_3 \tag{A.2}$$

Furthermore, leading partials $\mathbf{b}_3$ and $\mathbf{b}'_3$ modify the local stacking sequence of closed packed planes {111} from FCC to HCP. On the contrary, trailing partials $\mathbf{b}_2$ and $\mathbf{b}'_2$ remove the fault, restoring the original FCC lattice. Thereby, Shockley partial dislocations as in Eqs. (A.1) and (A.2) always enclose a stacking fault region, characterized by the presence of HCP sub-arrangements (Hull and Bacon, 2001) (see Fig. A.1b). Accordingly, the initiation of the plastic deformation can be associated to the HCP occurrence.

As regards the evolution of plastic deformation, it is strictly related to Shockley partials interactions. As a matter of fact, leading partials $\mathbf{b}_3$ and $\mathbf{b}'_3$ interact each other at the intersection of slip planes $(11\bar{1})$ and (111), yielding to a Lomer–Cottrell (LC) dislocation

$$\frac{B}{3}[110] = \frac{B}{3}[2\bar{1}1] + \frac{B}{3}[\bar{1}2\bar{1}] \tag{A.3}$$

that does not belong to a slip plane. As a result, such a LC dislocation is sessile and it acts as a barrier (the so-called Lomer–Cottrell lock (Hull and Bacon, 2001)) for any additional slipping process in planes $(11\bar{1})$ and (111), repulsing the remaining two trailing Shockley partials $\mathbf{b}_2$ and $\mathbf{b}'_2$. Accordingly, material behaviour in plastic regime strictly depends on the evolution of such a locking mechanism.

References

Allen, M.P., Tildesley, D.J., 1991. Computer Simulation of Liquids. Clarendon Press Oxford.

Amelang, J.S., Kochmann, D.M., 2015. Surface effects in nanoscale structures investigated by a fully-nonlocal energy-based quasicontinuum method. Mech. Mater. 90, 166–184.

Arico, A.S., Bruce, P., Scrosati, B., Tarascon, J.M., Van Schalkwijk, W., 2005. Nanostructured materials for advanced energy conversion and storage devices. Nat.Mater. 4 (5), 366–377.

Biener, J., Hodge, A.M., Hamza, A.V., Hsiung, L.M., Satcher, J.H., 2005. Nanoporous au: A high yield strength material. J. Appl. Phys. 97, 024301.

Biener, J., Hodge, A.M., Hayes, J.R., Volkert, C.A., Zepeda-Ruiz, L.A., Hamza, A.V., Abraham, F.F., 2006. Size effects on the mechanical behavior of nanoporous au. Nano Lett. 6, 2379–2382.

Borg, U., Niordson, C.F., Kysar, J.W., 2008. Size effects on void growth in single crystals with distributed voids. Int. J. Plastic. 24, 688–701.

Bringa, E.M., Traiviratana, S., Meyers, M.A., 2010. Void initiation in fcc metals: Effects of loading orientation and nanocrystalline effects. Acta Materialia 58, 4458–4477.

Daw, M.S., Baskes, M.I., 1984. Embedded-atom method: derivation and application to impurities, surfaces and other defects in metals. Phys. Rev. B 29, 6443–6453.

Dormieux, L., Kondo, D., 2010. An extension of gurson model incorporating interface stress effects. Int. J. Eng. Sci. 48, 575–581.

Dormieux, L., Kondo, D., 2013. Non linear homogenization approach of strength of nanoporous materials with interface effects. Int. J. Eng. Sci. 71, 102–110.

Duan, H.L., Wang, J., Huang, Z.P., Karihaloo, B.L., 2005. Eshelby formalism for nano-inhomogeneities. Proc. R. Soc. A 461, 3335–3353.

Duan, H.L., Wang, J., Huang, Z.P., Karihaloo, B.L., 2005. Size-dependent effective elastic constants of solids containing nano-inhomogeneities with interface stress. J. Mech. Phys. Solids 53, 1574–1596.

Farrissey, L., Ludwig, M., McHugh, P.E., Schmauder, S., 2000. An atomistic study of void growth in single crystalline copper. Comput. Mater. Sci. 18, 102–117.

Gologanu, M., Leblond, J.B., Devaux, J., 1993. Approximate models for ductile metals containing non-spherical voids in the case of axisymmetric prolate ellipsoidal cavities. J. Mech. Phys. Solids 41, 1723–1754.

Gologanu, M., Leblond, J.B., Perrin, G., Devaux, J., 1994. Approximate models for ductile metals containing non-spherical voids - case of axisymmetric oblate ellipsoidal cavities. J. Eng. Mater. Technol. 116, 290–297.

Goudarzi, T., Avazmohammadi, R., Naghdabadi, R., 2010. Surface energy effects on the yield strength of nanoporous materials containing nanoscale cylindrical voids. Mech. Mater. 42, 852–862.

Gurson, A.L., 1977. Continuum theory of ductile rupture by void nucleation and growth: Part i. - yield criterion and flow rules for porous ductile media. J. Eng. Mat. Technol. 99, 2–15.

Gurtin, M.E., Murdoch, A.I., 1975. Continuum theory of elastic material surfaces. Arch. Rational Mech. Anal. 57, 291–323.

Hakamada, M., Mabuchi, M., 2007. Mechanical strength of nanoporous gold fabricated by dealloying. Scripta Materalia 56, 1003–1006.

Hashin, Z., 1962. The elastic moduli of heterogeneous materials. J. Appl. Mech. 29, 143–150.

Higginbotham, A., Bringa, E.M., Marian, J., Park, N., Suggit, M., Wark, J.S., 2011. Simulations of copper single crystals subjected to rapid shear. J. Appl. Phys. 109, 063530.

Hill, R., 1948. A theory of the yielding and plastic flow of anisotropic metals. Proc. R. Soc. London A 193, 281–297.

Honeycutt, J.D., Andemen, H.C., 1987. Molecular dynamics study of melting and freezing of small lennard-jones clusters. J. Phys. Chem. 91, 4950–4963.

Horstemeyer, M.F., Baskes, M.I., Plimpton, S.J., 2001. Length scale and time scale effects on the plastic flow of FCC metals. Acta Materalia 49, 4363–4374.

Huang, M., Li, Z., Wang, C., 2005. Coupling effects of void size and void shape on the growth of prolate ellipsoidal microvoid. Acta Mechanica Sinica 21, 272–277.

Hull, D., Bacon, D.J., 2001. Introduction to Dislocations. Butterworth-Heinemann.

Jenkins, S.B., 2010. Nanoporous Materials: Types, Properties, and Uses. Nova Science Publishers.

Kelchner, C.L., Plimpton, S.J., Hamilton, J.C., 1998. Dislocation nucleation and defect structure during surface indentation. Phys. Rev. B 58, 11085.

Khan, A.S., Huang, S., 1995. Continuum Theory of Plasticity. John Wiley & Sons, New York.

Leblond, J.B., Perrin, G., Suquet, P., 1994. Exact results and approximate models for porous viscoplastic solids. Int. J. Plastic. 10, 213–235.

Lemarchand, E., Dormieux, L., Kondo, D., 2015. Lode's angle effect on the definition of the strength criterion of porous media. Int. J. Numer. Anal. Methods Geomech. 39 (14), 1506–1526.

Levenberg, K., 1944. A method for the solution of certain problems in least-squares. Q. Appl. Math. 2, 164–168.

Li, Z., Huang, M., 2005. Combined effects of void shape and void size-oblate spheroidal microvoid embedded in infinite non-linear solid. Int. J. Plastic. 21, 625–650.

Lu, G.Q., Zhao, X.S., Wei, T.K., 2004. Nanoporous materials: science and engineering. Imperial College Press.

Lubarda, V.A., 2011. Emission of dislocations from nanovoids under combined loading. Int. J. Plastic. 27, 181–200.

Lubarda, V.A., Schneider, M.S., Kalantar, D.H., Remington, B.A., Meyers, M.A., 2004. Void growth by dislocation emission. Acta Materialia 52, 1397–1408.

Lubliner, J., 2008. Plasticity Theory. Dover Publications Inc., Mineola, New York.

Marian, J., Knap, J., Ortiz, M., 2004. Nanovoid cavitation by dislocation emission in aluminum. Phys. Rev. 93.

Marian, J., Knap, J., Ortiz, M., 2005. Nanovoid deformation in aluminum under simple shear. Acta Materialia 53, 2893–2900.

Marquardt, D., 1963. An algorithm for least-squares estimation of nonlinear parameters. SIAM J. Appl. Math. 11, 431–441.

Menetrey, P.H., Willam, K.J., 1995. Triaxial failure criterion for concrete and its generalization. ACI Struct. J. 92, 311–318.

Mi, C., Buttry, D.A., Sharma, P., Kouris, D.A., 2011. Atomistic insights into dislocation-based mechanisms of void growth and coalescence. J. Mech. Phys. Solids 59, 1858–1871.

Michel, J.C., Suquet, P., 1992. The constitutive law of nonlinear viscous and porous materials. J. Mech. Phys. Solids 40 (4), 783–812.

Mishin, Y., Farkas, D., Mehl, M.J., Papaconstantopoulos, D.A., 1999. Interatomic potentials for monoatomic metals from experimental data and ab initio calculations. Phys. Rev. B 59, 3393.

Monchiet, V., Cazacu, O., Charkaluk, E., Kondo, D., 2008. Macroscopic yield criteria for plastic anisotropic materials containing spheroidal voids. Int. J. Plastic. 24, 1158–1189.

Monchiet, V., Kondo, D., 2012. Exact solution of a plastic hollow sphere with a mises-schleicher matrix. Int. J. Eng. Sci. 51, 168–178.

Monchiet, V., Kondo, D., 2013. Combined voids size and shape effects on the macroscopic criterion of ductile nanoporous materials. Int. J. Plastic. 43, 20–41.

Moshtaghin, A.F., Naghdabadi, R., Asghari, M., 2012. Effects of surface residual stress and surface elasticity on the overall yield surfaces of nanoporous materials with cylindrical nanovoids. Mech. Mater. 51, 74–87.

Needs, R.J., Godfrey, M.J., Mansfield, M., 1991. Theory of surface stress and surface reconstruction. Surface Sci. 242, 215–221.

Plimpton, S.J., 1995. Fast parallel algorithms for short-range molecular dynamics. J. Comput. Phys. 117, 1–19.

Pogorelko, V.V., Mayer, A.E., 2016. Influence of titanium and magnesium nanoinclusions on the strength of aluminum at high-rate tension: Molecular dynamics simulations. Mater. Sci. Eng. 662, 227–240.

Ponte Castaneda, P., 1991. The effective mechanical properties of nonlinear isotropic composites. J. Mech. Phys. Solids 39, 45–71.
Rittel, D., Ravichandran, G., Venkert, A., 2006. The mechanical response of pure iron at high strain rates under dominant shear. Mater. Sci. Eng. 432, 191–201.
Ruestes, C.J., Bringa, E.M., Stukowski, A., Rodriguez Nieva, J.F., Bertolino, G., Tang, Y., Meyers, M.A., 2013. Atomistic simulation of the mechanical response of a nanoporous body-centered cubic metal. Scripta Materialia 68, 817–820.
Seppala, E.T., Belak, J., Rudd, R.E., 2004. Effect of stress triaxiality on void growth in dynamic fracture of metals: A molecular dynamics study. Phys. Rev. B 69, 134101.
Shabib, I., Miller, R.E., 2009. Deformation characteristics and stress-strain response of nanotwinned copper via molecular dynamics simulation. Acta Materialia 57, 4364–4373.
Stukowski, A., 2010. Visualization and analysis of atomistic simulation data with OVITO-the open visualization tool. Model. Simul. Mater. Sci. Eng. 18, 015012.
Stukowski, A., 2012. Structure identification methods for atomistic simulations of crystalline materials. Model. Simul. Mater. Sci. Eng. 20, 4.
Subramaniyan, A.K., Sun, C., 2008. Continuum interpretation of virial stress in molecular simulations. Int. J. Solids Struct. 45, 4340–4346.
Tang, T., Kim, S., Horstemeyer, M.F., 2010. Molecular dynamics simulations of void growth and coalescence in single crystal magnesium. Acta Materalia 58, 4742–4759.
Traiviratana, S., Bringa, E.M., Benson, D.J., Meyers, M.A., 2008. Void growth in metals: Atomistic calculations. Acta Materalia 56, 3874–3886.
Tvergaard, V., Needleman, A., 1984. Analysis of the cup-cone fracture in a round tensile bar. Acta metallurgica 32, 157–169.
Verlet, L., 1967. Computer "experiments" on classical fluids. i. thermodynamical properties of lennard-jones molecules. Phys. Rev. 159, 98.
Zhang, W., Wang, T.J., 2007. Effect of surface energy on the yield strength of nanoporous materials. Appl. Phys. Lett. 90, 063104.
Zhang, W., Wang, T.J., Chen, X., 2010. Effect of surface/interface stress on the plastic deformation of nanoporous materials and nanocomposites. Int. J. Plastic. 26, 957–975.
Zhao, K.J., Chen, C.Q., Shen, Y.P., Lu, T.J., 2009. Molecular dynamics study on the nano-void growth in face-centered cubic single crystal copper. Comput. Mater. Sci. 46, 749–754.